An Observing System Simulation Experiment for the Calibration and Validation of the Surface Water Ocean Topography Sea Surface Height Measurement Using In Situ Platforms

Jinbo Wang,[a] Lee-Lueng Fu,[a] Bo Qiu,[b] Dimitris Menemenlis,[a] J. Thomas Farrar,[c] Yi Chao,[d] Andrew F. Thompson,[e] and Mar M. Flexas[e]

[a] *Jet Propulsion Laboratory, California Institute of Technology, Pasadena, California*
[b] *University of Hawai'i at Mānoa, Honolulu, Hawaii*
[c] *Woods Hole Oceanographic Institution, Woods Hole, Massachusetts*
[d] *Remote Sensing Solutions, Monrovia, California*
[e] *California Institute of Technology, Pasadena, California*

ABSTRACT

The wavenumber spectrum of sea surface height (SSH) is an important indicator of the dynamics of the ocean interior. While the SSH wavenumber spectrum has been well studied at mesoscale wavelengths and longer, using both in situ oceanographic measurements and satellite altimetry, it remains largely unknown for wavelengths less than ~70 km. The Surface Water Ocean Topography (SWOT) satellite mission aims to resolve the SSH wavenumber spectrum at 15–150-km wavelengths, which is specified as one of the mission requirements. The mission calibration and validation (CalVal) requires the ground truth of a synoptic SSH field to resolve the targeted wavelengths, but no existing observational network is able to fulfill the task. A high-resolution global ocean simulation is used to conduct an observing system simulation experiment (OSSE) to identify the suitable oceanographic in situ measurements for SWOT SSH CalVal. After fixing 20 measuring locations (the minimum number for resolving 15–150-km wavelengths) along the SWOT swath, four instrument platforms were tested: pressure-sensor-equipped inverted echo sounders (PIES), underway conductivity–temperature–depth (UCTD) sensors, instrumented moorings, and underwater gliders. In the context of the OSSE, PIES was found to be an unsuitable tool for the target region and for SSH scales 15–70 km; the slowness of a single UCTD leads to significant aliasing by high-frequency motions at short wavelengths below ~30 km; an array of station-keeping gliders may meet the requirement; and an array of moorings is the most effective system among the four tested instruments for meeting the mission's requirement. The results shown here warrant a prelaunch field campaign to further test the performance of station-keeping gliders.

1. Introduction

The Surface Water Ocean Topography (SWOT) mission aims to measure both the land water and ocean topography with an unprecedented horizontal resolution. The mission's satellite will carry a Ka-band Radar Interferometer (KaRIN) designed to yield high spatial resolutions over two swaths of 50 km with a 20-km gap centered at the nadir track (Durand et al. 2010; Fu and Ubelmann 2014). This paper focuses only on the ocean component. The high-resolution two-dimensional ocean topography measurements will enable us to study the upper-ocean dynamics and the associated heat and tracer transports therein, which are important processes in the climate system (Klein et al. 2015).

We are interested in the sea surface height (SSH) component that was governed by ocean eddies and high-frequency internal waves (referred to as *steric height* and explained in section 4). As a result, the steric height is referred to as the ground truth. It is shown in section 5c that after removing the atmospheric loading and the barotropic signals reflected in the bottom pressure, the sea surface height measured by satellite is equivalent to the steric height. The measurement error is consequently defined as the difference between satellite measurements (after the inverted barometer and barotropic tidal corrections) and steric height in this paper.

Corresponding author: Dr. Jinbo Wang, jinbo.wang@jpl.nasa.gov

For the first time, the mission's requirement is specified in terms of the cross-track averaged *wavenumber spectrum* of measurement errors (Fig. 1). The baseline error requirement (the red line in Fig. 1) is an approximation of the summation of all the noises and errors, including a constant white noise that dominates at small wavelengths and a colored noise that represents residual geophysical errors, orbit errors, and attitude restitution errors, and that dominates at longer wavelengths. More details can be found in the SWOT science requirements document (Rodríguez 2016). This unprecedented mission requirement in the wavenumber space imposes challenges on the SSH calibration and validation (SSH CalVal) task. While the onboard conventional nadir altimeter can be used for wavelengths longer than 150 km (appendix A), the SSH CalVal becomes more complex at 15–150 km (also referred to as *the SWOT scales*) because of the presence of high-frequency oceanic motions. It is therefore crucial to provide the ground truth for the steric height at the SWOT scales for the CalVal purpose.

While it is theoretically simple to reconstruct the steric height from ocean interior temperature T and salinity S measurements, no existing observational network can provide a synoptic wavenumber spectrum at these wavelengths. Here we perform an observing system simulation experiment (OSSE) using a high-resolution global ocean simulation to help design a new observing system to fulfill the mission's requirement.

We focus on resolving 15–150-km wavelengths. The shortest wavelength 15 km requires the minimum measurement resolution to be 7.5 km (resolve 15 km as the Nyquist wavelength). To resolve the longest wavelength (150 km), we need to have 20 points of measurements, given that the distance between measurements is determined by the Nyquist wavelength, that is, 150 km/7.5 km = 20. Here we regard 20 measuring locations along the swath as the baseline configuration. We selected four oceanographic instruments that can perform the SSH reconstruction, either from direct measurements of ocean interior T/S or from a proxy that is correlated to steric heights (see section 4). The pressure-sensor-equipped inverted echo sounder (PIES) reconstructs the steric height using an empirical relationship between the time for an acoustic pulse to travel through the water column and the steric height itself. Underway conductivity–temperature–depth (UCTD), moorings with CTDs, and gliders can directly measure T/S profiles to retrieve the steric height.

The outline of the paper is as follows. In section 2 we discuss the SWOT CalVal orbit and the two
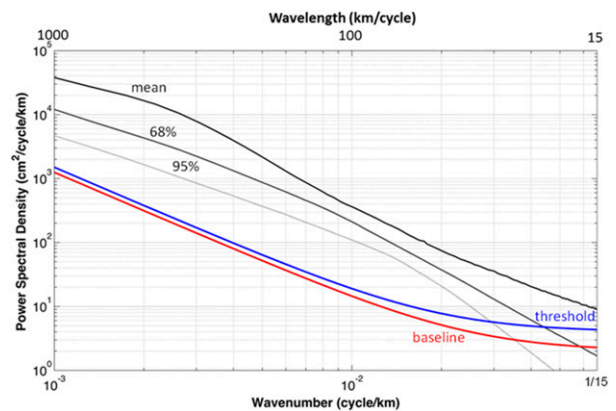

FIG. 1. SSH baseline requirement spectrum (red curve) as a function of wavenumber represented by an empirical function $E(k) = 2 + 0.00125k^{-2}$, where k represents the wavenumber, and the threshold requirement (blue curve). Shown for reference is the global mean SSH spectrum estimated from the *Jason-1* and *Jason-2* observations (thick black line), the lower boundary of 68% of the spectral values (thin black line), and the lower boundary of 95% of the spectral values (gray line). Intersections of the two dotted lines with the baseline spectrum at ~15 km (68%) and ~30 km (95%) determine the resolving capabilities of the SWOT measurement. Respective resolutions for the threshold requirement are ~25 km (68%) and ~35 km (95%) (Rodríguez 2016).

potential CalVal sites. Section 3 includes descriptions of the numerical simulation used as a representation of the true SSH (the "nature run"). In section 4 we discuss the basis for reconstructing the steric height in the nature run and the characteristics of the steric height variability therein. In section 5 we describe the OSSE methodology, including the description of the simulation of the four instruments and the synthetic SWOT SSH. Since PIES and UCTD are found to be inadequate in meeting the CalVal requirement, we focus on moorings and gliders. Results are shown in section 6, where we diagnose SSH from the simulated glider and mooring measurements. Discussion and conclusions are presented in section 7.

2. The SWOT orbit and two potential sites for CalVal

The SWOT CalVal will occur during the 90-day calibration phase in a one-day repeat orbit (Fig. 2) after the instrument checkout phase when the onboard configuration of the instruments has been settled (Fu et al. 2012). This fast sampling phase significantly expedites the data acquisition for the instrument calibration and its performance validation, and it minimizes the calibration time for the transition to the nominal mission phase. The 1-day repeat fast sampling increases the temporal resolution at the cost
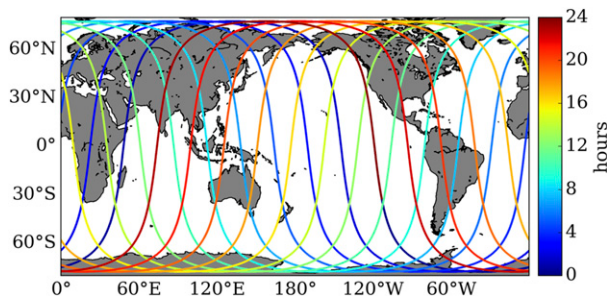
FIG. 2. One-day repeat orbit during the CalVal phase color coded by time.

of spatial coverage. Even though the data collected during these 90 days can still be used for the scientific application, the CalVal is the main focus. The large gaps between the satellite tracks without any measurement are not a concern. For the purpose of the SSH CalVal, an in situ field campaign will be launched concurrently to provide the ground truth of the regional synoptic SSH at the CalVal site.

The satellite orbits Earth 14 times during a one-day period, leaving 25.7143°-wide gaps between adjacent tracks in the low and midlatitudes. The 14 crossover locations between ascending and descending tracks along 35.7°N are ideal for CalVal because they double the daily satellite overflights. The following two potential sites were selected along 35.7°N: 35.7°N, 125.40°W off California (C-site), and 35.7°N, 22.54°W near the Azores Islands (A-site) (Fig. 3). Both locations are within oceanic eastern boundary currents and have weak mesoscale eddies.[1] The steric height variation in these regions is about 5 cm, an order of magnitude smaller than that in western boundary currents. It is worth noting that although it is easier to conduct in situ experiments in these less energetic regions, it is harder to separate the weak SSH signals from noisy satellite measurements.

3. Simulation of the ocean by a numerical model

Observations such as expendable bathythermograph (XBT) have been used to demonstrate the validity of altimetry measurement at large scales (>100 km) (e.g.,

---

[1] The crossover location near the Gulf Stream was originally considered, but it was found to be unsuitable. The swift currents can cause 1) excessively large horizontal displacements in moorings' horizontal locations and vertical displacements of the moored instruments and 2) large glider drifts. A moored instrument at 50 m might be displaced to 500 m when the ocean current speed reaches over 1 m s^{-1}, even though the mooring could be designed to reduce this effect at an additional cost. Strong currents also cause large horizontal drift for gliders, undermining their station-keeping capability.

Gilson et al. 1998). SSH responds to rapidly changing ocean processes including internal tides and gravity waves, whose contribution becomes dominant when the scales get smaller (~50 km). To make an informed decision on the SWOT in situ CalVal, we use a state-of-the-art high-resolution ocean general circulation simulation developed by the Jet Propulsion Laboratory in collaboration with the Massachusetts Institute of Technology based on the MITgcm (Marshall et al. 1997) and conducted an OSSE study. We refer to this simulation as the nature run.

The nature run is a global ocean simulation with a 1/48° horizontal resolution. The model solves the hydrostatic primitive equations using the Boussinesq approximation. The 1/48° horizontal grid is about 1.8 km at the CalVal latitude (35.7°N). The model has 90 vertical levels, with about 1-m vertical resolution at the surface and 30 m down to 500 m, for better resolving the upper-ocean processes. The model has zero parameterized horizontal diffusivity. In the vertical direction, the K-profile parameterization (KPP; Large et al. 1994) is used for boundary layer turbulent mixing. The model is forced by the 6-hourly ERA-Interim atmosphere reanalysis. In addition, a synthetic surface pressure field consisting of the 16 most dominant tidal constituents (A. Chaudhuri 2014, personal communication) is used to dynamically mimic the tidal forcing (e.g., Ponte et al. 2015). The inclusion of tidal forcing results in an energetic field of internal tides and gravity waves, which represent a substantial component in the SSH wavenumber spectrum at the SWOT scales (section 4b). The clear contribution from internal waves to the kinetic energy over the 10–40-km range in both this simulation and observations has been previously reported in Rocha et al. (2016) in the Drake Passage region in the Southern Ocean. In a recent paper, Savage et al. (2017) compared several tide-resolving numerical simulations with observations (McLane profiler) and reported that this simulation outperforms other models in representing supertidal frequencies. The accurate reproduction of the high-frequency SSH variability is therefore crucial for a realistic OSSE. The simulation saves hourly snapshots of SSH, velocity, temperature, and salinity fields for one year. This OSSE uses 90 days of model output, starting from 1 June 2012.

The nature run has been compared to observations. Favorable conclusions have been drawn by several independent studies. Rocha et al. (2016) compared the shipboard ADCP data collected in the Drake Passage (Southern Ocean) to the equivalent velocity from the model and found a good model-data agreement for both rotational and divergent motions separated
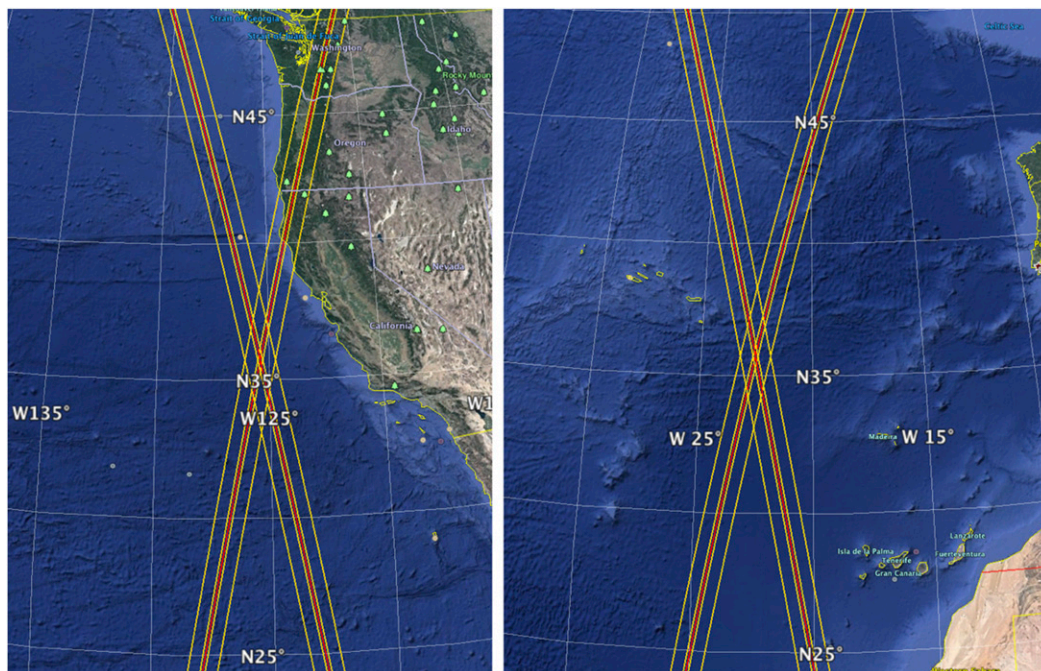
FIG. 3. SWOT swath in the (left) California Current System and (right) Azores Current. Nadir location (red lines) and edge of the swath (yellow lines). Ascending and descending tracks form a diamond shape centered at 35.55°N, 125.40°W for the C-site and 35.7038°N, 22.5390°W for the A-site, which are ideal locations for the SWOT SSH CalVal.

following the one-dimensional Helmholtz decomposition (Bühler et al. 2014). C. Wunsch (2016, personal communication) compared the model velocity with the mooring ADCP velocity at D-site on the continental rise north of the Gulf Stream maintained by the Woods Hole Oceanographic Institution and concluded that the model output was in agreement with observations within a factor of 2 at that location in terms of kinetic energy in internal tides.

As an example we have analyzed 25 repeat ADCP surveys from 3°–34°N along 137°E conducted by the Japan Meteorological Agency during the period 2004–16 (Qiu et al. 2017). The nature run reproduces the locations of the distinct zonal currents. The kinetic energy is reproduced within the same amplitude as the observed (Fig. 4). Further model–data comparisons are under development as a part of the effort of the High-Resolution Numerical Modeling Working Group within the SWOT science team.

Even though we do not have in situ measurements for a direct validation of the simulation at the potential CalVal sites, the results given above have proven the mode's fidelity. While the results in this paper provide useful guidance, the extent to which the model reproduces the real ocean at the CalVal sites is an important question that still needs to be addressed.

4. The model SSH

a. SSH budget

The hydrostatic balance is a good approximation for the ocean at the 15-km scale and larger. The nature run implements the hydrostatic approximation and the model SSH can be computed from the hydrostatic equation,

$$\frac{\partial p}{\partial z} = -\rho g; \quad \rho = \rho_o + \rho',$$

where p is the pressure, ρ is the potential density, ρ_o is the reference potential density ($1027.5 \, \text{kg} \, \text{m}^{-3}$), ρ' is the potential density anomaly, and g is the gravity of Earth. Integrating the above equation in the vertical gives

$$p_a - p_b = -\rho_0 g(\eta + H) - \int_{-H}^{\eta} \rho' g \, dz,$$

where p_b is the ocean bottom pressure, p_a is the atmospheric surface pressure, η is the SSH referenced to $z = 0$, and $-H$ is the depth of the ocean. After rearrangement, one obtains

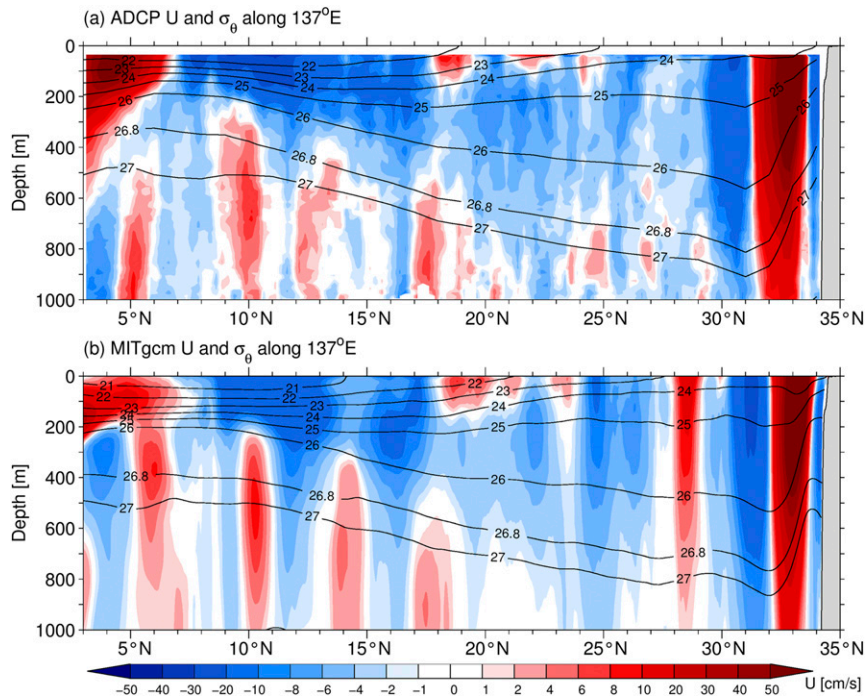$$\eta = \frac{p_b'}{\rho_o g} - \frac{p_a}{\rho_o g} - \int_{-H}^{0} \frac{\rho'}{\rho_o} \, dz, \tag{1}$$

FIG. 4. Latitude–depth sections of time-mean zonal velocity (colored contours) and density (black contours in θ) along 137°E from (a) JMA repeat ADCP surveys of 2004–16 and (b) the nature run. Note that contour scales are nonlinear and that colors denote east (red) and westward (blue) flows.

where $p_b' \overset{\text{def}}{=} p_b - g\rho_0 H$ represents the bottom pressure anomaly, and the term $\int_0^\eta (\rho'/\rho_0)\, dz$ has been neglected because $\eta \ll H$. The three terms on the right-hand side of Eq. (1) represent the contributions from the bottom pressure (η^b), the atmospheric pressure loading [the inverted barometer (IB) effect η^a], and the steric height (ξ, related to dynamic height by a factor of g), respectively. In the following, we use ξ^{z1-z2} to denote the steric height as a result of the water column sandwiched between depths at $z1$ and $z2$. For example, ξ^{0-500} represents the steric height as a result of the upper 500 m.

One necessary verification of the model's fidelity in simulating SSH is to check the SSH balance in Eq. (1). Checking the balance also helps us understand the dominant factors that modulate SSH signals.

Figure 5 shows the time series of each term in Eq. (1) sampled near the C-site. At high frequencies, the dominant terms are between η and η^b, mainly reflecting the high-frequency barotropic signals on the order of $O(10^2)$ cm. At subinertial frequencies, all the low-pass filtered terms are largely reduced in amplitude. The SSH budget mainly reflects the IB effect (blue and cyan lines). The steric height ξ^{0-H} is approximately $O(5)$ cm. The η^b is reduced to a negligible level at about 5% of the steric height on the SWOT scales (green line). The

residual (gray line) is almost zero, indicating the closed SSH budget in the model within the hydrostatic approximation.

The barotropic signals, the IB effect, and bottom pressure signals, even though of large amplitude, can be easily removed using a spatial filter as a result of their large-scale characteristics. We will discuss this point in section 5c.

b. The influence of inertia-gravity waves on SSH

The complexity of the SWOT ocean CalVal is mainly caused by the high-frequency energetic inertia-gravity waves on the SWOT scales (15–150 km). Our knowledge of SSH wavenumber spectra is mostly derived from satellite altimetry available during the past decades, which is unfortunately dominated by noise at wavelengths less than ~100 km (Xu and Fu 2012). While observations have been used to study the wavenumber spectra of kinetic/potential energy and tracer variance (Katz 1973; Samelson and Paulson 1988; Ferrari and Rudnick 2000; Wang et al. 2010; Callies and Ferrari 2013; Rocha et al. 2016), the wavenumber spectra of SSH at the SWOT scales are poorly known.

A few recent studies based on numerical simulations have shown that the inertia-gravity waves have a clear
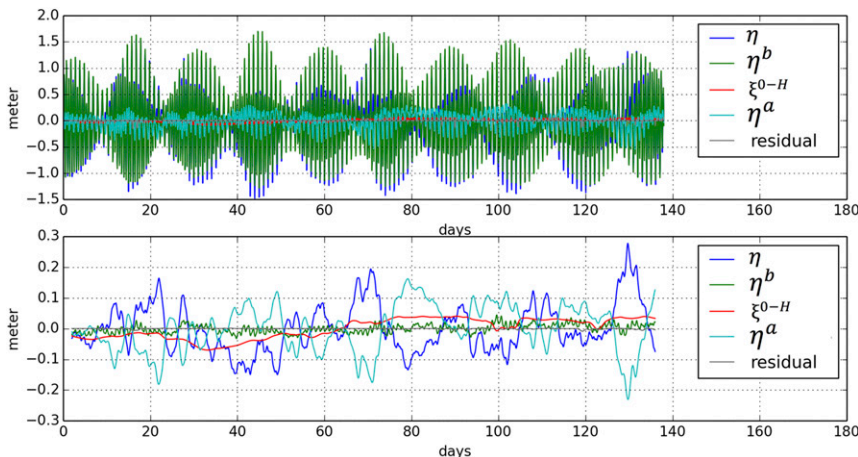
FIG. 5. Time series of each term in Eq. (1): η (blue), η^b (green), full-depth steric height ξ^{0-H} (red), η^a as a result of atmospheric forcing (cyan), and the residual (gray). (top) Hourly data and (bottom) low-pass filtered (>1 day) data.

contribution to SSH over the SWOT scales (Richman et al. 2012; Rocha et al. 2016). The SSH wavenumber spectrum near the C-site in the nature run is shown here as an example (Fig. 6). The super- and subinertial components are taken to approximate the wave motions and the balanced motions, respectively. It is clear that waves are much more energetic than balanced motions over a major part of the SWOT scales at this location. This wave dominance on the submesoscale scale kinetic energy over the tested regions is not likely a model artifact considering several recent studies based on ADCP velocity observations also report similar wave dominance in kinetic energy wavenumber spectra (Qiu et al. 2017).

These energetic high-frequency waves impose difficulty in capturing synoptic SSH signal and warrant high-frequency sampling strategies, which eliminate the usage of the platforms that cannot cover a 150-km distance within a short period of time. Based on the sensitivity studies (results not shown), we conclude that we need to measure the 150-km distance within about 1 h to capture the synoptic dynamics.

c. The upper-ocean dominance in SSH variability

We use the following index to measure the contribution of the upper ocean:

$$r(z, k) = 1 - \frac{S_{\xi^{z-H}\xi^{z-H}}(k)}{S_{\xi^{0-H}\xi^{0-H}}(k)},$$

where $S_{xx}(k)$ represents the power spectrum density of x as a function of wavenumber k, ξ^{z-H} represents the steric height as a result of the water column sandwiched between z and H. Consequently, $r(z_0, k_0) = 1$ means that

ξ^{0-z_0} can explain 100% the full-depth steric height ξ^{0-H} at k_0, or equivalently the ocean beneath z_0 has no contribution to the steric height anomaly. One caveat is that ξ^{z-H} sometimes has a strong negative correlation with ξ^{0-z}, so they compensate each other and either of the two can exceed ξ^{0-H}, resulting in $r < 0$. The negative correlation can be understood as the anticorrelation between the density anomalies of the upper $(0–z)$ and the lower $(z–H)$ layers. It is a possibility, but it does not occur in our case. The $r(z, k)$ at the C-site is >70% for all wavenumbers if $z < -580$ m (Fig. 7), indicating the upper-ocean dominance in the steric height component of the SSH. However, it is still a question whether the remaining 30% signal leads to errors larger than the CalVal requirement.
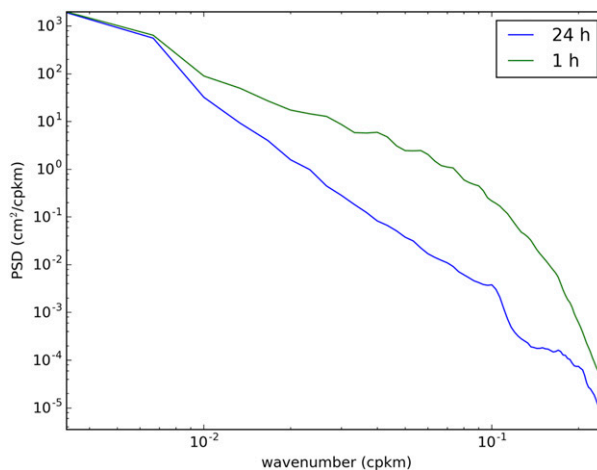

FIG. 6. Wavenumber spectrum of the hourly η (green) and the low-pass filtered (>24 h) version (blue).
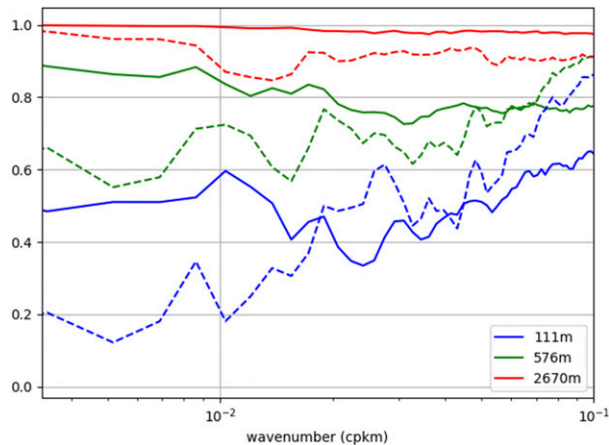
FIG. 7. Contribution of the upper-ocean steric height to the full-depth steric height defined by the parameter $r(z, k)$ explained in the main text; $r(z_0, k_0) = 1$ means that the steric height between the sea surface and z_0 can explain 100% of the full-depth steric height at wavenumber k_0. Each line represents a function $r(z, k)$ at a certain depth denoted in the legend. The solid (dashed) lines represent results at C-site (A-site).

The $r(-580 \, m, k)$ at the A-site (dashed green line) is smaller than that at the C-site (solid green line) for wavelengths larger than 15 km, indicating that we need a deeper sampling at the A-site.

5. The OSSE methodology

We consider the nature run as the real ocean and use it to simulate the true SSH measured by the SWOT satellite and the in situ instruments, that is, PIES, UCTD, mooring, and glider. It is worth noting that even though the model has a 1/48° horizontal resolution, the ocean physics are resolved at scales larger than grid scale, ~10 km at the latitude of the CalVal site. The in situ observing system measures either the ocean temperature and salinity for calculating the partial-depth steric height or the acoustic travel time to infer the steric height. The comparison of the true SSH to the SSH derived from in situ measurements is conducted in wavenumber space.

a. The SWOT SSH simulation

We use the SWOT ocean simulator (Gaultier et al. 2016) to interpolate the model SSH onto the SWOT along-track swath without adding measurement noise. The interpolated data have a horizontal resolution of 2 km × 2 km. The CalVal sites are located at points where the ascending and descending tracks cross (Fig. 3). The OSSE in this study is based on only the ascending tracks.

b. Simulated instruments

In our search for candidate instruments, we first ruled out passive platforms, such as Argo floats, because of the lack of station-keeping capability, and considered only fixed or controllable platforms. PIES and a single-boat UCTD were the first two tested instruments because of their light weight and low cost, but they were found to be inadequate in meeting the CalVal requirement for the target region. For PIES, the uncertainties of ~5 cm in the conversion of the acoustic travel time to steric height are too high for the SWOT requirement (appendix B). While the energetic mesoscale eddies can be resolved by PIES, submesoscale features are too weak to be reconstructed from PIES measurement (appendix B). For UCTD, a single UCTD-carrying boat needs about 10 h to complete a 150-km transect. It is too slow to capture the synoptic SSH wavenumber spectra, which have high-frequency variability (time scale of several hours). In the following, we skip the discussion of PIES and UCTDs, and focus on only the simulations of moorings and gliders.

1) MOORING

We place a number N of CTDs at depths $z = z_i$, $i = 0, \ldots, N - 1$ for each mooring. The first instrument is placed at $z_0 = -50$ m, a common practice for subsurface moorings. The distance between two CTD instruments is denoted as $\Delta z_i = z_{i-1} - z_i$, $i = 1, \ldots, N - 1$. We linearly interpolate model potential temperature and salinity onto the CTD depth to generate synthetic mooring measurements.

The measurement noise of the CTDs is represented by a Gaussian random process. We assumed the CTD instrument would be similar to Sea-Bird Scientific model SBE-37SI, which has a stated accuracy of ±0.002°C and ±0.003 mS cm^{-1} (roughly ±0.0024 psu). The standard deviation of the noise in a 5-min sample is taken to be 0.01°C and 0.02 psu for temperature and salinity, respectively, which are larger than the manufacture's stated accuracy to account for additional measurement errors in the field, such as those caused by biofouling of conductivity cells. For the hourly averaged quantity, the noise amplitude is scaled by $\sqrt{1/12}$ (averaging 12 samples per hour).

After the noise is added to the sampled CTD temperature and salinity, we calculate the potential density according to Jackett and Mcdougall (1995). The steric height from the synthetic mooring data is then calculated as

$$\xi_M = \frac{1}{\rho_0} \sum_{i=0}^{N-1} \rho_i' \Delta_i z^f,$$

where $\rho_i{}'$ is the density deviation from $\rho_0 = 1027.5 \, \mathrm{kg \, m^{-3}}$ (used by the model) at z_i and $\Delta_i z^f$ represents the layer thickness for the ith CTD measurement centered at z_i (f represents the grid size between the cell face, which is different from Δz_i). The thickness of the first layer is taken as $\Delta_0 z^f = 1.5 \Delta z_1$. The thickness of the last layer is taken as $\Delta_{N-1} z^f = \Delta z_{N-1}$. The interior layer thickness is

$$\Delta_i z^f = \frac{\Delta z_i + \Delta z_{i+1}}{2}, \quad i = 1, \ldots, N - 2.$$

2) GLIDER

A glider is an autonomous underwater vehicle that has been increasingly used in the field of oceanography to measure the upper-ocean properties. It makes repeated dives down to a preset depth while moving forward by controlling its buoyancy and pitch angle. Gliders have been used to perform station keeping to function as virtual profiling moorings (Hodges and Fratantoni 2009; Rudnick et al. 2013). The glider speed is between 20 and $25 \, \mathrm{cm \, s^{-1}}$, which is too small to maneuver against swift currents but is large enough to ensure station keeping in quiescent regions such as oceanic eastern boundaries. Station-keeping gliders can usually stay within 3-km distance to target over the quiescent regions (Branch et al. 2017).

For this OSSE we simulate the trajectories of station-keeping gliders using the three-dimensional velocity field of the nature run. The gliders are set to have a 60° dive angle, a 520-m dive depth (depth of a model grid near 500 m), and $21.7 \, \mathrm{cm \, s^{-1}}$ vertical velocity. This combination gives horizontal and absolute velocities of 12.5 and $25 \, \mathrm{cm \, s^{-1}}$, respectively, with a V-shaped (two profiles along ascending and descending paths) dive cycle of less than 2 h. Because the ocean vertical velocity influences the glider's vertical movement, the exact period of each diving cycle varies. The vertical sampling rate is set to every 5 m.

The simulation of the glider measurement is essentially the same as the one used for the moorings. The only difference is that the glider is a single moving platform and records only point measurements along its path in four dimensions. Let us denote the glider SSH $\xi_G^z(x, t)$, where the superscript z represents the glider's diving depth, $\mathbf{x}$ is the glider's surface location, and t is time. Given the glider's target location and the satellite overflight time (x^0, t^0), we need to compare the glider SSH to the truth in the form of a spectrum of the SSH difference as follows: $\xi_G^z(x^0, t^0) - \eta(x^0, t^0)$, where $\xi_G^z(x^0, t^0)$ is the glider SSH interpolated on to the target location (x^0, t^0).

We then interpolate the temperature and salinity of the nature run on to the glider trajectories. Linear interpolation is used in the horizontal direction and in time. The nearest-neighbor scheme is used in the vertical interpolation because the model layer is in general thicker than the glider's vertical sampling rate, so the model truth can be reproduced given an instantaneous snapshot.

Random instrument noise is added to the interpolated glider T/S profiles: 0.01°C for temperature and 0.01 for salinity (Damerell et al. 2016). These instrument Gaussian noises do not matter because the vertical integration operator in deriving SSH from T/S profiles significantly reduces their contribution (recall that the vertical resolution in glider measurement is 5 m and there are 104 data points in the upper 520 m). We do not consider the vertical tilt of the glider trajectory and use only the surface location for the glider SSH $\xi_G^z(\mathbf{x}, t)$. Figure 8 shows an example of a time series of a ξ_G^{520} and the associated frequency spectrum and coherence. It shows a good match between the glider SSH and ξ^{0-H}, although ξ_G^{520} has a weaker amplitude by a factor of ~1.5 at superinertial frequencies, indicating the possible SSH contribution of the deeper ocean below 520 m. The gliders' performance in the wavenumber spectrum is evaluated in section 6b.

c. SSH wavenumber spectrum

Both satellite and in situ measurements include signals of processes other than interior ocean dynamics, such as the IB effect, large-amplitude barotropic signals, and the bottom pressure signals related to water depth, which varies spatially. Once we have the simulated SWOT SSH, we need to filter out the SSH signals that are different from the dynamic component ξ. As mentioned in section 4, we found that those processes can be largely removed by preprocessing the data with temporal and spatial filters, which are shown as follows.

Let us denote the filtering operators in space and time as $\mathcal{L}_x$ and $\mathcal{L}_t$, respectively. We found that an operation $\mathcal{L}_t \mathcal{L}_x$ that removes the linear trend in both space (over 150 km) and time (of 90 days) is sufficient to remove the majority of the signals that are not related to steric height. Figure 9 shows a demonstration based on the nature run. We preprocessed the SWOT SSH $\eta(x, t)$ by the detrending operator: $\eta' = \mathcal{L}_x \mathcal{L}_t \eta(x, t)$. The excess energy in η (black line) is essentially removed by the filtering (blue line), resulting in an SSH field almost identical to the full-depth steric height ξ^{0-H} (red line). This demonstrates that removing the temporal linear trend and then the spatial linear
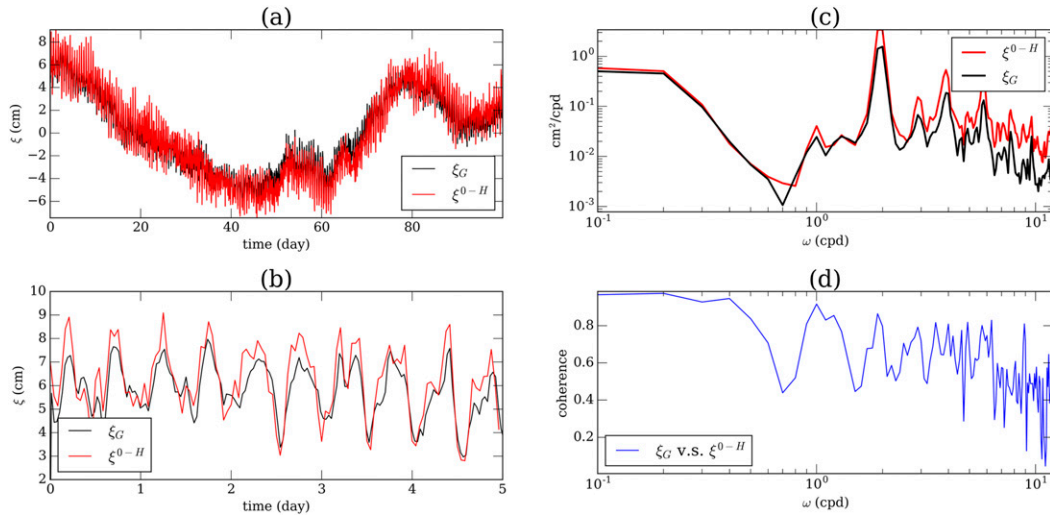
FIG. 8. Time series of ξ^{0-H} (red) and ξ_G^{0-520} (black) during (a) the full 100 days and (b) the first 5 days. (c) Frequency spectra of ξ_G^{0-520} and ξ^{0-H}, and (d) their coherence.

trend can effectively remove the IB effect and the bar-otropic signals. The large-spatial-scale diurnal signals are mostly removed, leaving the internal tides and waves at the semidiurnal and higher frequencies clearly captured by steric height. A caveat is that the nature run uses a 6-hourly atmospheric forcing field with a 0.14° horizontal resolution, which inherently lacks high-frequency and high-wavenumber variances, whose effect on SSH at the SWOT wavelengths is to be investigated using more suitable observations/simulations in future studies.

Removing the linear trend from the SSH time series at each instrument location also removes the stationary components, such as the bottom pressure related to the depth of the water column, also model drifts and the linear trend as a result of low-frequency seasonal variations. For the CalVal site of 150 km wide, removing the spatial linear trend can eliminate most of the IB effect and the bottom pressure signals, which are conventionally believed to be of large scale.

The bottom pressure contribution η^b is negligible compared to ξ^{0-H} after applying the filters. The ratio of the power spectral density between η^b and ξ^{0-H} is below 5% for all considered wavenumbers (figure not shown), indicating that the bottom pressure is less important for the CalVal purpose.

6. The design of an in situ observing system

To capture a synoptic SSH field at 15–150-km scales, the simplest design is to have an array of 20 sites uniformly

spaced on a 150-km-long section along the center of the SWOT swath (Fig. 10). The 20 sites ensure a Nyquist wavenumber of 1/15 cycles per kilometer (cpkm) and the synoptic SSH spectrum be captured by the mooring array. The real observing system will probably consist of a combination of moorings and gliders, but we test only the performance of these two instruments separately.

a. Mooring based

Two scenarios are evaluated with different numbers of CTDs for the mooring configuration. In the first scenario, we consider 20 CTDs placed in the upper 570 m. In the second scenario, we add six additional CTDs below 570 m to cover the deeper ocean down to 2670 m.
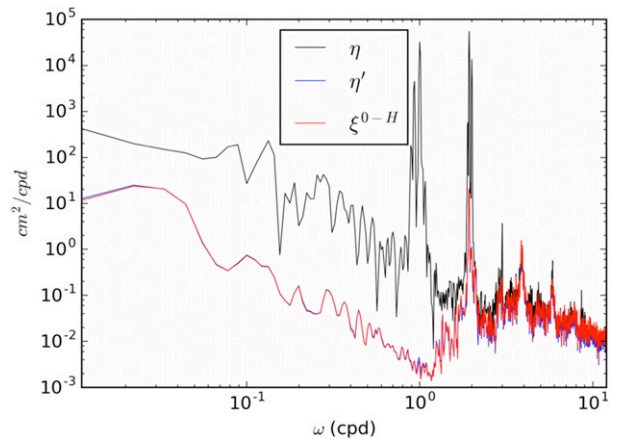

FIG. 9. Frequency spectra of the total SSH η (black line), the spatially linearly detrended SSH $\eta' = \mathcal{L}_x \mathcal{L}_t \eta$ (blue line), and ξ^{0-H} (red line).
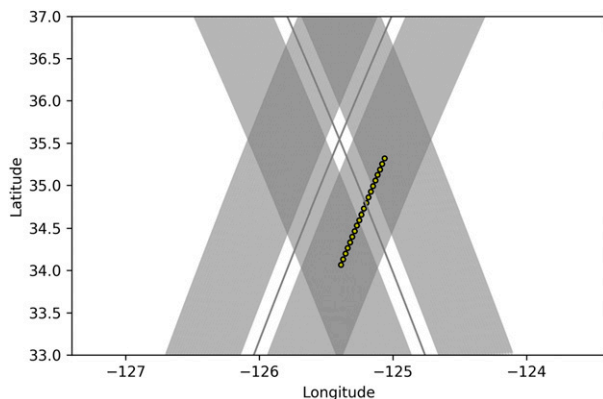
FIG. 10. Illustration of the positions of 20 moorings (yellow dots) on the background of the diamond shape of the ascending and descending swaths and nadir tracks (gray); 20 moorings are placed along the center of a swath over a 150-km distance.

The vertical placements of the mooring instruments are listed in Table 1. In addition to these two scenarios, an optimization test shows that we can reduce the number of instruments to 13 without sacrificing performance if the spatial correlation matrices of the density at different depths are known (appendix C).

Figure 11 shows the results of the mooring SSH at the two sites in the two scenarios. At the C-site (left panels), scenario 1, where only the upper ocean between 50 and 570 m is sampled (top left), yields a mooring reconstruction, ξ_M^{0-570} (green line), very close to the truth, η (black line). The spectrum of the difference between ξ_M^{50-570} and η is much smaller than η itself (blue). The error-to-signal ratio defined as $[S_{(\xi_M-\eta)(\xi_M-\eta)}(k)/S_{\eta\eta}(k)]$ is about 0.3 or less for all wavenumbers (purple line). Adding six additional instruments between 570 and 2670 m in scenario 2 increases the accuracy of the mooring SSH ξ_M (Fig. 11, bottom left).

At the A-site (Fig. 11, right panels), scenario 1 yields an error (purple lines) about 30% of the original signal for all wavenumbers (Fig. 11c). Scenario 2 shows a ratio exceeding 0.3 for wavelength smaller than 40 km (Fig. 11d). These results appear to be much worse than the results at the C-site. It is because the A-site needs deeper samplings (Fig. 7). However, the absolute errors (blue lines) are of similar amplitude for the two sites. The large error-to-signal ratio for the A-site is because of the relative weaker eddy activities. This is well illustrated by comparing to the SWOT baseline error requirement (red line). The SSH spectral level at the C-site is much higher than the baseline error except for a small wavelength near 15 km, but the SSH spectral level at the A-site is below the baseline error on scales < 25 km. So, even though the error-to-signal ratio is large there, the absolute error represented by $\xi_M - \eta$ is still

less than the baseline requirement. This means that if the SSH field is much weaker than the baseline requirement, the satellite measurement is dominated by noise. In such a case, in situ measurements are useful in providing a reference for a rest ocean. All measurements can be categorized as errors for the purpose of CalVal.

Note that the error-to-signal ratio is flatter in scenario 1 at the A-site (Fig. 11c) than in the other three cases (Figs. 11a,b,d). It is because the contribution of the deep ocean below 570 m is different between the two sites. At the C-site, the upper ocean above 570 m can sufficiently represent the steric height variance of the full depth, so the error is small relative to the original signal. However, at the Azores site, the deep ocean has more significant contribution to the steric height variation (Fig. 7), so the errors become relatively larger without accounting for the deeper ocean in scenario 1. The error-to-signal ratio thus becomes flatter in Fig. 11c. This indicates that the depth we need to measure at the Azores site has to be deeper than that at the California site.

In summary, at the C-site, the CTD measurements of an array of 20 moorings along the SWOT swath will allow for reconstruction of the true SSH spectrum with less than 30% error if only the upper ocean (50–570 m) is measured. Placing six additional CTDs between 570 and 2670 m reduces the error to less than 10% at wavelengths longer than 40 km. At the A-site, even though the error-to-signal ratio is large, the absolute error is similar to that of the C-site and meets the baseline requirement.

There are uncertainties caused by the swing of a mooring line by ocean currents, resulting in the deepening of the CTDs especially the top one. We tested two additional scenarios based on scenarios 1 and 2, but we placed the first CTD at 100 m. This is an aggressive assumption, as the upper-ocean currents in the A- and C-sites are too weak to induce a 50-m vertical displacement of the topmost CTD (based on empirical data not shown here). The results are similar (figure not shown), suggesting that the vertical mooring motion should not be a concern for the in situ observing system at the two potential sites. However, a caveat is that the model resolves only physics at ~10-km scales; the effect of horizontal displacement is probably underestimated in this simulation and needs to be investigated in the future.

b. Glider based

We design the glider system based on the mooring system by substituting each mooring with one station-keeping glider, that is, 20 gliders covering the same 150-km line.

TABLE 1. Parameters of the mooring configurations.

Scenario	Depth of the first CTD (m)	Depth of the deepest CTD (m)	No. of instruments	Δz_i (m)
1	50	570	20	5, 5, 5, 5, 5, 5, 10, 10, 10, 10, 15, 15, 30, 40, 50, 50, 50, 100, 100
2	50	2670	26	5, 5, 5, 5, 5, 5, 10, 10, 10, 10, 15, 15, 30, 40, 50, 50, 50, 100, 100, 200, 300, 300, 300, 500, 500

Figure 12a shows the surface locations (dots) of the 20 gliders over the course of 100 days (color) on a background of the SWOT swath (gray). Data from the first 90 days are used in the following calculation. Figure 12b zooms in one of the gliders. During the 100 days, gliders can perform station keeping within a 1-km distance most of the time, but they are occasionally swept up to 6 km away from the target by sporadic eddies and filaments.

Gliders perform worse than moorings. Glider SSH ξ_G^{0-520} is generally weaker than ξ^{0-H}. The maximum error is less than a factor of 2 larger than the requirement at the 40-km wavelength (Fig. 13). The gliders' performance may be potentially improved by further optimizations. For example, the ocean velocity from a regional ocean forecast can be used to navigate gliders to improve its station-keeping performance (M. Troesch et al. 2017, unpublished manuscript), and the SSH component caused by internal tides, which dominate the 20–70 km wavelengths, can be better reconstructed by considering

the coherent, hence predictable, tidal component. We will focus on the glider optimization in another study.

Our conclusion is that a system with gliders may potentially meet the CalVal requirement but further tests are needed. At this stage we do not pursue more sophisticated glider OSSEs because we have reached the limit of the nature run, which has a ~2-km horizontal resolution and hourly output. To acquire more confidence in the glider's performance, we would require a nature run with much higher resolution and/or a prelaunch field campaign with gliders, neither of which is available at the writing of this paper.

7. Conclusions

At scales 15–150 km, the SSH wavenumber spectrum itself is not well known, and no existing observing system can be used to carry out a realistic test. Here we take advantage of a state-of-the-art high-resolution global
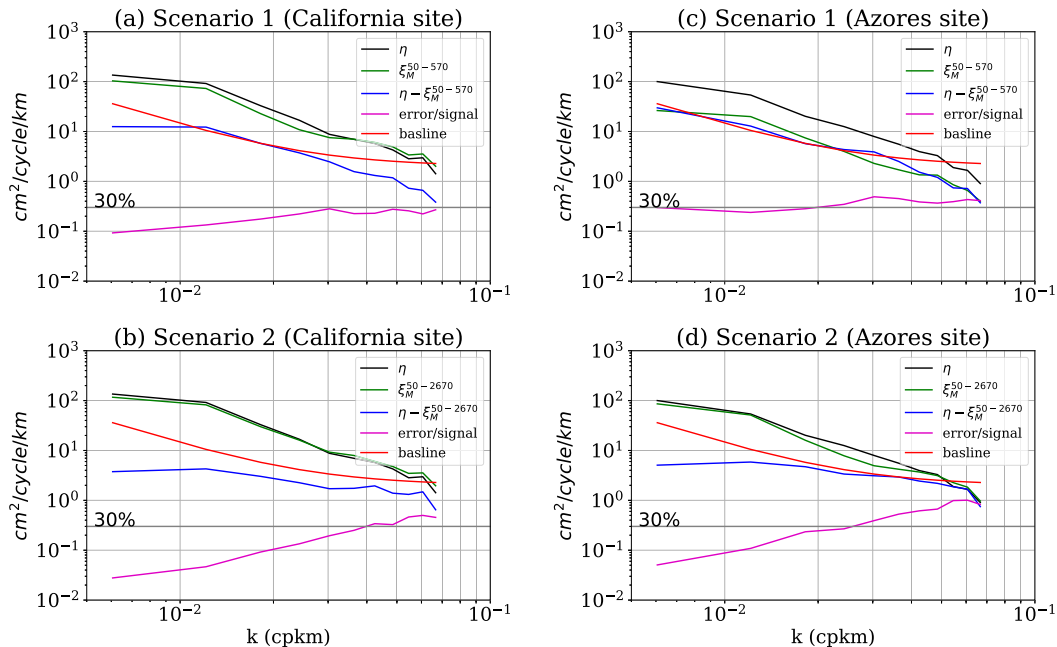

FIG. 11. Results at the (left) C-site and (right) A-site in (top) scenario 1 and (bottom) scenario 2. Power spectrum density of the true SSH anomaly η' (black), the mooring reconstruction ξ_M (green), the residual $(\eta - \xi_M)$ (blue), the error-to-signal ratio (purple), and the baseline (red). Visual guide of the 30% (0.3) level (horizontal line).
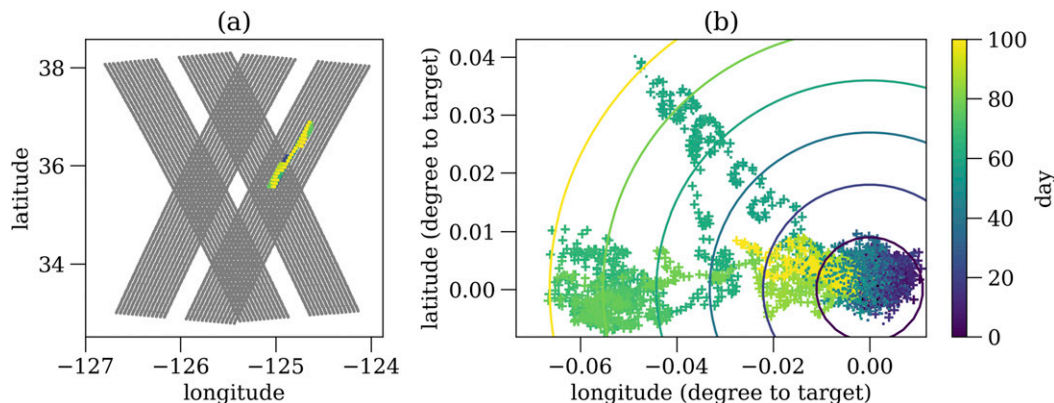
FIG. 12. (a) Surface positions of 20 gliders over the course of 100 days (color) overlaid on top of the SWOT swaths at the crossover location. Locations of the glider are off the center of the swath and are different from the illustration in Fig. 10, but they do not affect the conclusion. Final plan for the location of the instruments is still to be determined and not the focus here. (b) Surface positions of glider 1. Target location is marked (black symbol). Distances to target with a 1-km interval are indicated (circles; outer circle marks 6 km to target).

ocean simulation and perform an observing system simulation experiment for the SWOT SSH CalVal.

The SWOT mission requirement was defined based on the cross-track averaged SSH measurement. A prudent choice is to place an instrument array along the center of a swath, where the SWOT measurement performance is best. The cross-track variability of the measurement error is dominated by the KaRIN random noise (Fig. 14), which can be readily determined from the actual measurement. We can then use the information in these functions (Fig. 14) to extrapolate the difference between the SWOT and in situ observations along the instrument array to other cross-track locations in order to estimate the cross-track averaged measurement error.

For constructing the observing array, we fixed the number of measuring locations to be 20, which is the minimum number to cover 15–150-km wavelengths, and tested the ability of four different oceanographic instruments—PIES, UCTD, mooring, and glider—to meet the SWOT SSH CalVal baseline requirement.

An array of 20 moorings is capable of recovering a wavenumber spectrum accurate enough to serve as a reference to satellite measurements. The 20 moorings may potentially be replaced by station-keeping gliders, even though an individual glider cannot capture high-frequency variability ($>1/2$ cph). Our simulation of the glider's performance shows that an array of 20 gliders does not strictly meet the requirement but that the errors are less than a factor of 2 of the requirement. Gliders may potentially have reduced errors through optimizations to meet the mission requirement. We expect a better SSH reconstruction with more gliders. The nature run also appears to overestimate the internal

wave/tide energy in low-latitude locations (B. Arbic 2016, personal communication). Glider-derived velocity may improve the glider's station-keeping capability by short-term forecast of the ocean current. The results in this study warrant further investigation into the fidelity of the nature run and the glider performance with the aid of either a higher-resolution simulation or a prelaunch field campaign. An ongoing field campaign was carried out to test the glider's station keeping during June–July of 2017. The results will be reported in a separate paper. Finally, we use this study to build the concept for the SWOT in situ SSH CalVal. The final design will probably include a combination of platforms
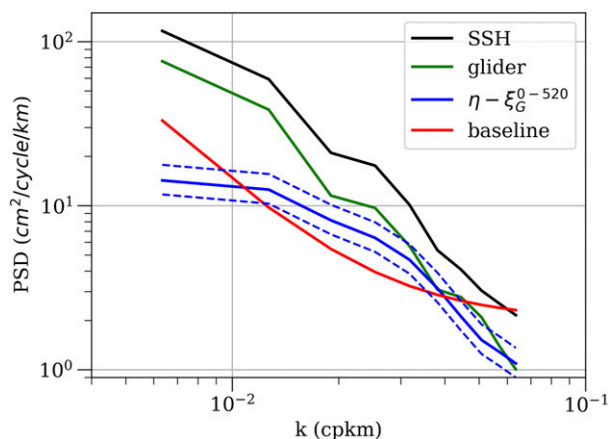

FIG. 13. Wavenumber spectra of SSH η (black), ξ_G^{0-520} (green), their difference (solid purple), and SWOT CalVal baseline (red) in the wavenumber space; 95% confidence interval for the error spectrum, assuming the 90 daily snapshots are independent (two dashed lines).
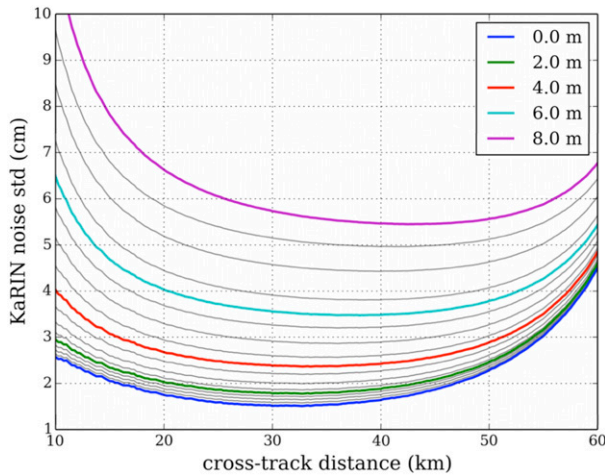
FIG. 14. KaRIN random error, instrument plus wave effects (surfboard effects), as a function of cross-track ground range for various significant wave height values ranging from 0 to 8 m plotted with a 0.5-m increment.

with a more complex observing pattern to meet the mission requirement.

APPENDIX A

Using the Onboard Nadir Altimeter for the Long-Wavelength CalVal

One of the applications of the SWOT onboard nadir altimeter is for the calibration and validation of the KaRIN sea surface topography at long wavelengths.

While the nadir altimeter is well known to resolve ~100-km wavelengths, it is still a question at what scale the SWOT nadir altimeter can be used for the CalVal purpose. The centers of the two swaths are 35 km off nadir. This introduces a major representation error, that is, using a nadir altimeter to represent the off-nadir KaRIN swaths. We use the MITgcm high-resolution simulation (1/48°) to quantify the scale above which the nadir altimeter can be used for SWOT SSH CalVal.

Denote the SWOT SSH measurements as $\eta(s, n)$, where s and n represent the along-track and cross-track directions, respectively. The nadir SSH is denoted as $\eta(s, 0)$. The KaRIN measurements at the center of the two swaths are $\eta(s, \pm 35\,\text{km})$. To investigate the nadir altimeter's performance in the CalVal of SWOT KaRIN measurements, we compare the spectra and the associated difference of the following two quantities:

$$\frac{1}{2}[\eta(s, 35\,\text{km}) + \eta(s, -35\,\text{km})],$$

$$\eta(s, 0) + \epsilon,$$

where ϵ is the added random noise with zero mean and 2-cm^2 variance. The first quantity represents the true SSH at two midswaths interpolated onto the nadir track. The second quantity represents the nadir altimeter SSH with 2-cm^2 noise.

The results are shown in Figs. A1 and A2. The spectra are calculated based on 90 daily measurements starting from 1 June 2012. Figure A1 shows that the error (green line) is comparable to the original signal (blue and purple lines) at 150 km (the gray vertical line). At wavelengths longer than 150 km, the error becomes much less than the original signal. The coherence (Fig. A2) confirms that 150 km is the transition wavelength for the nadir altimeter to be used as the CalVal reference.

To conclude, based on the analysis of the MITgcm 1/48° simulation at the California CalVal site, the onboard nadir altimeter can be used as the CalVal reference for wavelengths longer than 150 km.

APPENDIX B

Simulation of PIES

The acoustic travel time from the seafloor to the sea surface can be used to infer the depth changes in the main thermocline (Rossby 1969). As the steric height is intrinsically linked with the interior temperature and salinity, acoustic travel time can be used to reconstruct the steric height through an empirical relationship (Watts and Rossby 1977).
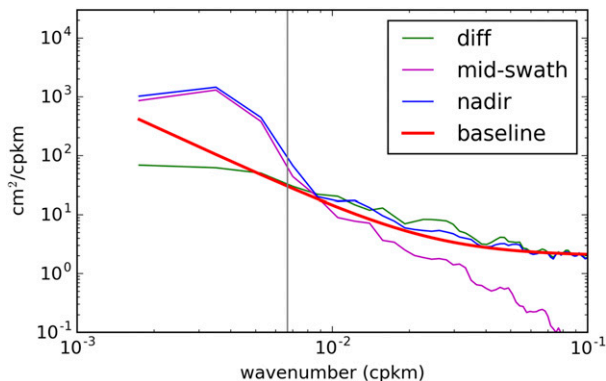
FIG. A1. Spectrum of $\eta(s, 0) + \epsilon$ (blue line), $(\eta(s, 35\,\mathrm{km}) + \eta(s, -35\,\mathrm{km}))/2$ (purple line), their difference (green line), and SWOT baseline requirement (red line).

FIG. A2. Coherence between $\eta(s, 0) + \epsilon$ and $(\eta(s, 35\,\mathrm{km}) + \eta(s, -35\,\mathrm{km}))/2$. Coherence starts to drop quickly at 200 km, becomes 0.6 at 150 km, and almost zero at 100 km.

PIES carries two instruments: a pressure recorder that measures the bottom pressure p_b and an inverted echo sounder that measures the round-trip acoustic travel time τ of self-generated acoustic pulses. An empirical relationship between τ and the full-depth steric height ξ^{0-H} has been then used to reconstruct the steric height, which has been demonstrated to be nearly linear (Watts and Rossby 1977).

To use the model results to simulate PIES, we first use the "*temp*" subroutine in the seawater package (http://www.teos-10.org/) to convert the model potential temperature θ to in situ temperature T, which is then used to compute the sound speed using "*svel*." The travel time of a sound pulse is computed as

$$\tau = 2 \sum_{k=1}^{N_z} \Delta z_k / c(T, S, p),$$

where N_z is the total number of model layers, Δz_k is the layer thickness of the kth layer (the first layer includes η), $c(T, S, p)$ is the sound speed as a function of in situ temperature T, salinity S, and pressure p.

The travel time τ is first temporally detrended, then fit to ξ^{0-H}. The empirical relationship, the lookup curve, that converts τ to ξ is constructed as an empirical second-order polynomial deduced from a least squares solution of $\xi_P^{0-4500} \approx f(\tau)$, where $z = 4500$ m following the procedure described in Baker-Yeboah et al. (2009). Figure B1 shows a typical lookup curve (red line) constructed from the relationship between ξ_P^{0-4500} and τ (black dots) in the Gulf Stream region (left panel) and California Current region (right panel) based on random samples of the model output. The misfits between the data and the polynomial curve are about 5 cm for both regions, which is typical (R. Watts 2016, personal communication).
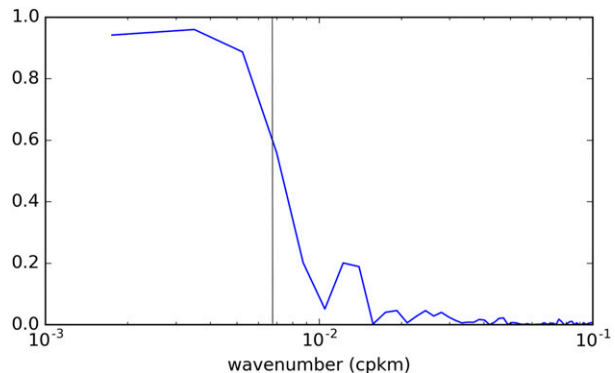
The coherence analysis shows that PIES cannot capture the variability at wavelengths below 100 km, where coherence falls below 0.4 (Fig. B2). With the same ~5-cm uncertainty, the performance of PIES in the California Current region is worse than in the Gulf Stream region (figure not shown).

The results shown here should be considered as the best scenario because we have not considered adding instrument and measurement noises. Even in this best scenario, PIES SSH has insufficient accuracy for meeting the SWOT SSH CalVal requirement.

APPENDIX C

Mooring Optimization

The mooring configuration can be optimized in terms of the number and locations of CTDs. One key assumption in using a limited number of CTDs in calculating the full-depth steric height is that the ocean can be partitioned into discretized layers with uniform water property in each layer. Layers adjacent to each other covary to an extent to be approximated as a thicker uniform layer, which is usually thinner in the upper ocean and thicker in the deep ocean as a result of the intrinsic surface-intensified ocean dynamics. The extent to which the ocean at a certain depth covaries with its adjacent depths can be measured by the correlation matrix. As a result, we can use the correlation matrix as a guide for the discretization.

The correlation matrix based on the spatial structure from an array of 20 moorings is calculated as

$$\sum_{ij} = \overline{\mathrm{corr}(\rho_i, \rho_j)}, \quad i, j \in (0, \ldots, N-1),$$

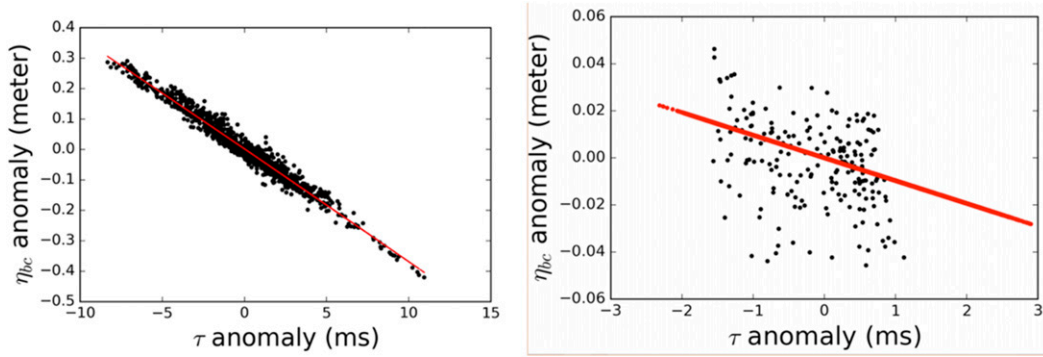where "corr" represents the Peterson correlation operation; N is the total number of the discretized layers

FIG. B1. Scatterplots of the full-depth steric height ξ^{0-4500} vs acoustic τ from PIES. Term τ is calculated from model temperature and salinity profiles (left) in the Gulf Stream region and (right) at the C-site. The red lines show the Lookup curve derived from a second-order polynomial fit to the black dots. Both ξ^{0-4500} and τ are anomalies from a temporal linear trend. Anomalies are large for the Gulf Stream region as a result of strong mesoscale activities but small for the California region as a result of the weaker mesoscale activities. It indicates that PIES works better in Gulf Stream region than in California Current.

($N = 90$ in the nature run); $\rho_{i,j}(x)$ is the density at the layers i and j, respectively, as a function of along-track distance x; and the overbar represents the 90-day average. The correlation matrix calculated based on the time series at a single location leads to the same results (not shown).

The correlation matrix for the C-site is shown in Fig. C1. The dark shading marks the locations where $\sum_{ij} > 0.9$, showing that the covarying layers are thinner in the upper ocean and thicker in the deeper ocean. We can use the depth range within $\sum_{ij} > 0.9$ for the discretization to eliminate the redundant CTDs in the mooring configurations.

Here we show one example of the optimized mooring configuration at the C-site. A total of 13 CTDs are used in contrast to 20 and 26 in the main text. The first CTD is still at 50 m, but the distance between two CTDs are $\Delta z_i = [20, 25, 38, 72, 62, 123, 231, 254, 221, 408, 450, 600]$,

which is derived from the correlation matrix. We see that the optimized layer thicknesses are larger than 5 m and are not a monotonic function of depth, which are different from our intuitive guess used in the main text. Figure C2 shows that the 13 CTDs with the optimized depths have a similar performance to scenario 1, where 20 instruments are used (Fig. 11).

This is a demonstration that, with enough prior knowledge of the ocean variability in the targeted CalVal region, represented by the correlation matrix, we can optimize the mooring configuration and reduce the required number of CTDs. A caveat is that our calculation is based on perfect knowledge of the correlation matrix, which does not usually apply to the real ocean.
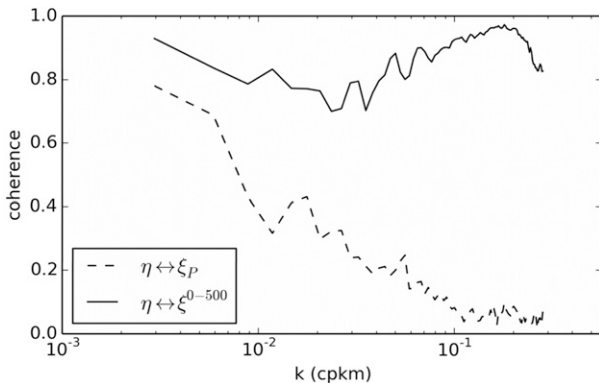

FIG. B2. Coherence of η' with PIES reconstruction ξ_P (dashed line) and ξ^{0-500} (solid line); at shorter wavelengths (<100 km), ξ_P loses its coherence with η'.
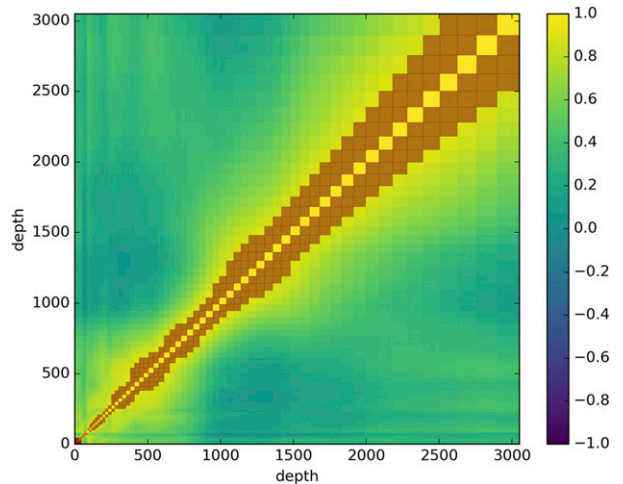

FIG. C1. Spatial correlation matrix of the potential density as a function of depth; definition can be found in the text.
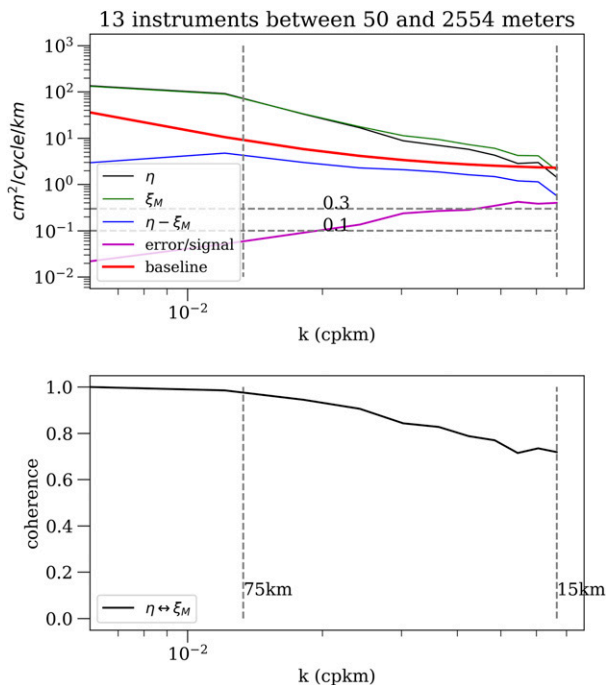
FIG. C2. (top) As in Fig. 11, but for the mooring configuration with 13 CTDs. (bottom) Coherence between the SSH and the mooring reconstruction.

This highlights the benefit of a prelaunch field campaign at the CalVal site.

REFERENCES

Baker-Yeboah, S., D. R. Watts, and D. A. Byrne, 2009: Measurements of sea surface height variability in the eastern South Atlantic from pressure sensor–equipped inverted echo sounders: Baroclinic and barotropic components. *J. Atmos. Oceanic Technol.*, **26**, 2593–2609, https://doi.org/10.1175/2009JTECHO659.1.

Branch, A., M. Troesch, M. Flexas, A. F. Thompson, J. Ferrara, Y. Chao, and S. Chien, 2017: Station keeping with an autonomous underwater glider using a predictive model of ocean currents. *Proc. 26th Int. Joint Conf. on Artificial Intelligence (IJCAI-17)*, Melbourne, VIC, Australia, IJCAI, University of Technology Sydney, and Australian Computer Society, 5 pp., https://ai.jpl.nasa.gov/public/papers/branch_ijcai2017_station.pdf.

Bühler, O., J. Callies, and R. Ferrari, 2014: Wave–vortex decomposition of one-dimensional ship-track data. *J. Fluid Mech.*, **756**, 1007–1026, https://doi.org/10.1017/jfm.2014.488.

Callies, J., and R. Ferrari, 2013: Interpreting energy and tracer spectra of upper-ocean turbulence in the submesoscale range (1–200 km). *J. Phys. Oceanogr.*, **43**, 2456–2474, https://doi.org/10.1175/JPO-D-13-063.1.

Damerell, G., K. Heywood, A. Thompson, U. Binetti, and J. Kaiser, 2016: The vertical structure of upper ocean variability at the Porcupine Abyssal Plain during 2012–2013. *J. Geophys. Res. Oceans*, **121**, 3075–3089, https://doi.org/10.1002/2015JC011423.

Durand, M., L.-L. Fu, D. P. Lettenmaier, D. E. Alsdorf, E. Rodríguez, and D. Esteban-Fernandez, 2010: The surface water and ocean topography mission: Observing terrestrial surface water and oceanic submesoscale eddies. *Proc. IEEE*, **98**, 766–779, https://doi.org/10.1109/JPROC.2010.2043031.

Ferrari, R., and D. L. Rudnick, 2000: Thermohaline variability in the upper ocean. *J. Geophys. Res.*, **105**, 16 857–16 883, https://doi.org/10.1029/2000JC900057.

Fu, L.-L., and C. Ubelmann, 2014: On the transition from profile altimeter to swath altimeter for observing global ocean surface topography. *J. Atmos. Oceanic Technol.*, **31**, 560–568, https://doi.org/10.1175/JTECH-D-13-00109.1.

——, D. Alsdorf, R. Morrow, E. Rodríguez, and N. Mognard, Eds., 2012: SWOT: The Surface Water and Ocean Topography mission: Wide-swath altimetric measurement of water elevation on Earth. California Institute of Technology Jet Propulsion Laboratory JPL Publ. 12-05, 228 pp.

Gaultier, L., C. Ubelmann, and L.-L. Fu, 2016: The challenge of using future SWOT data for oceanic field reconstruction. *J. Oceanic Atmos. Technol.*, **33**, 119–126, https://doi.org/10.1175/JTECH-D-15-0160.1.

Gilson, J., D. Roemmich, B. Cornuelle, and L.-L. Fu, 1998: The relationship of TOPEX/POSEIDON altimetric height to steric height and circulation in the North Pacific. *J. Geophys. Res.*, **103**, 27 947–27 965, https://doi.org/10.1029/98JC01680.

Hodges, B., and D. Fratantoni, 2009: A thin layer of phytoplankton observed in the Philippine Sea with a synthetic moored array of autonomous gliders. *J. Geophys. Res.*, **114**, C10020, https://doi.org/10.1029/2009JC005317.

Jackett, D. R., and T. J. Mcdougall, 1995: Minimal adjustment of hydrographic profiles to achieve static stability. *J. Atmos. Oceanic Technol.*, **12**, 381–389, https://doi.org/10.1175/1520-0426(1995)012<0381:MAOHPT>2.0.CO;2.

Katz, E., 1973: Profile of an isopycnal surface in the main thermocline of the Sargasso Sea. *J. Phys. Oceanogr.*, **3**, 448–457, https://doi.org/10.1175/1520-0485(1973)003<0448:POAISI>2.0.CO;2.

Klein, P., and Coauthors, 2015: White paper on mesoscale / submesoscale dynamics in the upper ocean. JPL Publ., 13 pp.

Large, W. G., J. C. McWilliams, and S. C. Doney, 1994: Oceanic vertical mixing: A review and a model with a nonlocal boundary layer parameterization. *Rev. Geophys.*, **32**, 363–403, https://doi.org/10.1029/94RG01872.

Marshall, J., C. Hill, L. Perelman, and A. Adcroft, 1997: Hydrostatic, quasi-hydrostatic, and nonhydrostatic ocean modeling. *J. Geophys. Res.*, **102**, 5733–5752, https://doi.org/10.1029/96JC02776.

Ponte, R. M., A. H. Chaudhuri, and S. V. Vinogradov, 2015: Long-period tides in an atmospherically driven, stratified ocean. *J. Phys. Oceanogr.*, **45**, 1917–1928, https://doi.org/10.1175/JPO-D-15-0006.1.

Qiu, B., T. Nakano, S. Chen, and P. Klein, 2017: Submesoscale transition from geostrophic flows to internal waves in the northwestern Pacific upper ocean. *Nat. Commun.*, **8**, 14055, https://doi.org/10.1038/ncomms14055.

Richman, J. G., B. K. Arbic, J. F. Shriver, E. J. Metzger, and A. J. Wallcraft, 2012: Inferring dynamics from the wavenumber spectra of an eddying global ocean model with embedded tides. *J. Geophys. Res.*, **117**, C12012, https://doi.org/10.1029/2012JC008364.

Rocha, C. B., T. Chereskin, S. T. Gille, and D. Menemenlis, 2016: Mesoscale to submesoscale wavenumber spectra in Drake Passage. *J. Phys. Oceanogr.*, **46**, 601–620, https://doi.org/10.1175/JPO-D-15-0087.1.

Rodríguez, E., 2016: Surface Water and Ocean Topography Mission project. Science Requirements Doc., Revision A, California Institute of Technology Jet Propulsion Laboratory Publ. JPL D-61923, 28 pp.

Rossby, T., 1969: On monitoring depth variations of the main thermocline acoustically. *J. Geophys. Res.*, **74**, 5542–5546, https://doi.org/10.1029/JC074i023p05542.

Rudnick, D. L., T. M. Johnston, and J. T. Sherman, 2013: High-frequency internal waves near the Luzon Strait observed by underwater gliders. *J. Geophys. Res. Oceans*, **118**, 774–784, https://doi.org/10.1002/jgrc.20083.

Samelson, R. M., and C. A. Paulson, 1988: Towed thermister chain observations of fronts in the subtropical North Pacific. *J. Geophys. Res.*, **93**, 2237–2246, https://doi.org/10.1029/JC093iC03p02237.

Savage, A. C., and Coauthors, 2017: Frequency content of sea surface height variability from internal gravity waves to me-soscale eddies. *J. Geophys. Res. Oceans*, **122**, 2519–2538, https://doi.org/10.1002/2016JC012331.

Wang, D.-P., C. N. Flagg, K. Donohue, and H. T. Rossby, 2010: Wavenumber spectrum in the Gulf Stream from shipboard ADCP observations and comparison with altimetry mea-surements. *J. Phys. Oceanogr.*, **40**, 840–844, https://doi.org/10.1175/2009JPO4330.1.

Watts, D. R., and H. T. Rossby, 1977: Measuring dynamic heights with inverted echo sounders: Results from MODE. *J. Phys. Oceanogr.*, **7**, 345–358, https://doi.org/10.1175/1520-0485(1977)007<0345:MDHWIE>2.0.CO;2.

Xu, Y., and L.-L. Fu, 2012: The effects of altimeter instrument noise on the estimation of the wavenumber spectrum of sea surface height. *J. Phys. Oceanogr.*, **42**, 2229–2233, https://doi.org/10.1175/JPO-D-12-0106.1.